

See discussions, stats, and author profiles for this publication at: <https://www.researchgate.net/publication/243375014>

Theoretical and Experimental Study of the Electronic Structures of MoO₃ and MoO₂

ARTICLE in THE JOURNAL OF PHYSICAL CHEMISTRY C · MARCH 2010

Impact Factor: 4.77 · DOI: 10.1021/jp9093172

CITATIONS

111

READS

207

6 AUTHORS, INCLUDING:



David O. Scanlon

University College London

116 PUBLICATIONS 2,084 CITATIONS

SEE PROFILE



Graeme W Watson

Trinity College Dublin

203 PUBLICATIONS 6,808 CITATIONS

SEE PROFILE



Russell G Egdell

University of Oxford

262 PUBLICATIONS 6,300 CITATIONS

SEE PROFILE

Theoretical and Experimental Study of the Electronic Structures of MoO₃ and MoO₂David O. Scanlon,[‡] Graeme W. Watson,^{*,‡} D. J. Payne,[§] G. R. Atkinson,[§] R. G. Egdel,^{†,§} and D. S. L. Law^{||}*School of Chemistry, Trinity College Dublin, Dublin 2, Ireland, Department of Chemistry, Inorganic Chemistry Laboratory, University of Oxford, South Parks Road, Oxford OX1 3QR, United Kingdom, and NCESS, Daresbury Laboratory, Warrington, Cheshire WA4 4AD, United Kingdom**Received: September 28, 2009; Revised Manuscript Received: December 8, 2009*

The geometric and electronic structures of MoO₃ and MoO₂ have been calculated using the generalized gradient approximation to density functional theory. The calculated cross-section weighted densities of states are compared with high-resolution X-ray photoemission spectra. There is very good agreement between the calculated structures and those determined previously by X-ray diffraction and between the computed densities of states and the present photoemission measurements. MoO₂ is shown to be a metallic material, as is found experimentally, but the Fermi level sits in a distinct trough in the density of states. Satellite peaks found in core photoemission spectra of MoO₂ are shown to derive from final state screening effects in this narrow band metallic material.

1. Introduction

Molybdenum forms two simple binary oxides, namely, MoO₃ and MoO₂.^{1,2} Formally MoO₃ is a 4d⁰ Mo(VI) compound, and the material is an insulator. A metastable β phase is known³ which adopts a ReO₃-like structure similar to that of WO₃. However, the thermodynamically favored α phase crystallizes in a unique orthorhombic crystal structure^{2,4,5} (space group *Pbnm*) with lattice constants $a = 3.962$ Å, $b = 13.855$ Å, and $c = 3.699$ Å. This structure is based on a series of bilayers that are oriented perpendicular to the [010] y axis as shown in Figure 1a. Each bilayer consists of two sublayers of distorted MoO₆ octahedra to give three crystallographically inequivalent oxygen sites. These involve singly coordinated (terminal) oxygen O(1), two-coordinate oxygen O(2), and three-coordinate oxygen O(3). Each O(1) oxygen is bonded to only one Mo atom by a very short Mo–O bond length of 1.67 Å. O(2) is 2-fold coordinated and located asymmetrically between two Mo centers with bond lengths of 1.73 and 2.25 Å. Lastly, the O(3) oxygen is symmetrically placed between two Mo centers in a sublayer with a bond distance of 1.94 Å and also connected to another Mo center in the other sublayer with a bond length of 2.33 Å,⁶ Figure 1b. Each bilayer interacts with the adjacent bilayer in the [010] direction through a weak noncovalent interaction, which is mainly van der Waals in origin.⁷ The onset of strong optical absorption in α -MoO₃ thin films is typically around 3.2 eV.^{3,8,9} However, polycrystalline or single-crystal material has a distinct yellow coloration, and the lowest absorption edge in single crystals is at 440 nm, corresponding to a lower band gap of 2.8 eV.¹⁰

MoO₃ has found widespread use in heterogeneous catalysis both as a “stand alone” material or when activated by deposition onto a suitable oxide support.¹¹ It has applications in hydrocracking¹² and desulfurization processes,¹³ metathesis,^{14,15} and reactions involving removal of nitrogen oxides¹⁶ and partial oxidation.¹⁷ MoO₃ is also used in the production of synthetic

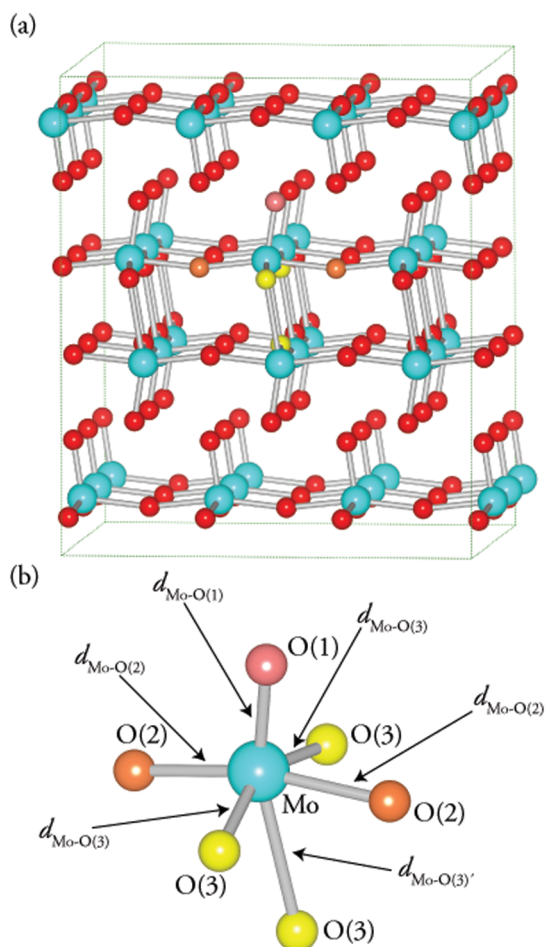


Figure 1. (a) Crystal structure of orthorhombic MoO₃ showing the layered structure along the (010) direction. (b) MoO₆ distorted octahedra highlighting the bond ordering.

* To whom correspondence should be addressed. E-mail: watsong@tcd.ie.

† E-mail: russell.egdel@chem.ox.ac.uk.

‡ Trinity College Dublin.

§ University of Oxford.

|| Daresbury Laboratory.

fibers¹⁸ and has received attention as a candidate material for electrochromic¹⁹ and photochromic²⁰ devices and as a possible material for mechanical logic gate development.²¹ Recently,

MoO₃ has also been proposed as a possible host for Li intercalation in Li-ion batteries.²²

Experimentally the electronic structure of MoO₃ has been examined by ultraviolet photoelectron spectroscopy (UPS), X-ray photoelectron spectroscopy (XPS), X-ray absorption spectroscopy (XAS), and resonant soft X-ray inelastic scattering (RIXS). A very detailed study by Firment and Ferretti²³ used LEED, XPS, UPS, and ELS to investigate stoichiometric and oxygen-deficient MoO₃ surfaces. They report that the valence bandwidth of MoO₃ is 7 eV and that the density of states has maxima at 1.5, 3.6, and 5.6 eV below the leading edge of the valence band.²³ A recent study by soft X-ray emission (XES) and RIXS by Learmonth et al.²⁴ measured the experimental oxygen 2*p* partial density of states, which showed peaks at ~1.9, ~2.7, ~4.5, and ~6 eV below the valence band maximum (VBM).²⁴

MoO₃ has been the subject of a number of theoretical studies. The Hartree–Fock (HF) method,⁷ ab initio density functional theory (DFT) applied to clusters,²⁵ local density approximation (LDA) approaches,²⁶ tight-binding-linear muffin tin orbital (TB-LMTO)²⁷ LDA calculations, linear augmented plane-wave (LAPW) techniques,²⁸ and calculations based on the generalized gradient approximation (GGA) with correction for onsite Coulombic interactions (GGA + *U*)²⁹ have all been used to model this system. Catlow and co-workers studied the electronic structure of MoO₃ using HF with an a posteriori DFT correction for the effect of electron correlation to investigate the bonding in the bulk structure and concluded that a weak attractive Coulombic force acts between adjacent bilayers.⁷ Tokarz-Sobieraj et al. used DFT cluster studies and UPS to examine the electronic structure of the system and suggested that the O(2) oxygen takes the place of the O(1) terminal oxygen that is initially removed during reduction.²⁵ Chen et al. used LDA to study the adsorption of hydrogen, methyl radicals, and nitric oxide at terminal oxygen vacancies on the (010) MoO₃ surface.^{26,30,31}

Coquet and Willock used GGA and GGA + *U* to study the effect of oxygen vacancies on the electronic structure of the (010) surface.²⁹ They highlight the need to deal with the self-interaction error (in this case using GGA + *U*) in systems where the excess electrons or holes produced upon defect formation are localized on the neighboring cation or anion sites.²⁹ In such systems, GGA has been shown to provide an accurate description of the electronic structure of the stoichiometric phase but fails in the description of nonstoichiometric systems.^{32–36}

MoO₃ can be reduced quite easily, and there are at least six stable Magnéli phases³⁷ leading to the lower stable oxide MoO₂, where the formal oxidation state is Mo(IV) and the electron configuration on Mo is 4*d*².³⁸ The Magnéli phases are of course mixed valence compounds. MoO₂ crystallizes in a monoclinic structure^{39,40} (space group *P2₁/c*) with lattice constants of *a* = 5.6109 Å, *b* = 4.8562 Å, and *c* = 5.6285 Å and a monoclinic angle of 120.95° as shown in Figure 2a. The structure is closely related to that of rutile, but the unit cell contains four MO₂ formula units as opposed to two for rutile itself.³⁹ The parent rutile structure is tetragonal and based on chains of MO₆ octahedra which share opposite edges along the crystallographic *c* axis. Each metal atom is surrounded by six oxygen atoms, while each oxygen is surrounded by three metal atoms at the corners of an equilateral triangle. The nearest M–M separation is equal to the lattice parameter *c*. The metal coordination is not strictly octahedral, and there are two distinct metal–oxygen bond lengths with a local metal site symmetry *D*_{2h}.⁴¹ In the distorted rutile structure of MoO₂, the Mo–Mo distances along

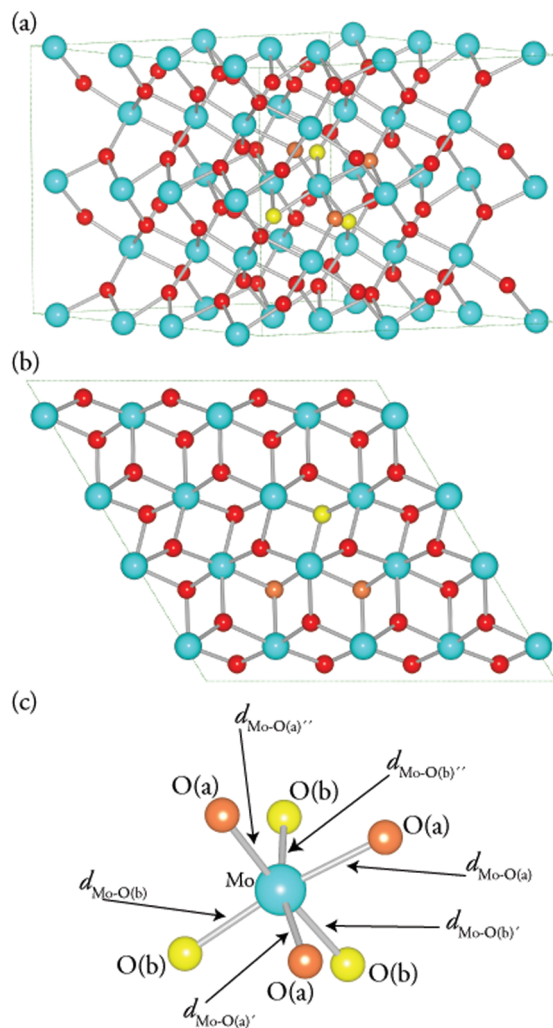


Figure 2. (a) Crystal structure of monoclinic MoO₂, (b) plan view of the distorted rutile structure, and (c) MoO₆ distorted octahedra highlighting the bond ordering.

the rutile *c* axis alternate to give two distinct metal to metal bond lengths of 2.51 and 3.02 Å. This also results in two distinct oxygen coordination environments, each with three M–O bond lengths³⁹ as shown in Figure 2c. The distorted structure adopted by MoO₂ is also found in WO₂, TcO₂, α-ReO₂, and the low-temperature forms of VO₂,³⁹ while the low-temperature form of NbO₂ is based on a closely related body-centered tetragonal structure with space group *I4₁/a*.^{42,43}

The driving force for structural distortion in MoO₂ and other *dⁿ* rutile-type dioxides was clarified by Goodenough.⁴⁴ The octahedral component of the ligand field experienced by the metal cations splits the 4*d* levels into *t*_{2g} and *e*_g sets. However, owing to the chain structure it is possible to distinguish between the single *t*_{2g} orbital in the plane defined by the shared octahedral edges (the *t*_{||} orbital in Goodenough's notation) and the other two *t*_{2g} orbitals which are perpendicular to this plane (the *t*_⊥ orbitals in Goodenough's notation). The *t*_{||} orbitals have lobes pointing along the *c* axis, and in distorted rutile oxides the *t*_{||} orbitals on adjacent metal centers can interact in a σ-like fashion to produce bonding and antibonding states. The band derived from in-phase *t*_{||} overlap is split away from the remaining bands associated with the less perturbed *t*_{2g} levels. In distorted *d*¹ compound such as the low-temperature polymorphs of VO₂ and NbO₂ the σ-bonding *t*_{||} band is fully occupied and the other *t*_{2g}-derived levels are empty, thus explaining the nonmetallic

behavior of these materials and also accounting for the driving force for distortion in terms of stabilization of two electrons per metal pair in a metal–metal bond. By contrast, in the d^2 oxide MoO_2 the one extra electron per metal cation partially populates the higher t_{1g} bands. MoO_2 therefore displays both metallic conductivity and metal–metal bonding. A refinement of the Goodenough model takes account of the possibility of π -type overlap between pairs of t_{1g} orbitals.^{45,46}

MoO_2 is less important in technological applications than MoO_3 , but it has been used as a catalyst for alkane isomerization^{47–51} or oxidation⁵² reactions and as a gas sensor.⁵³ It is also a promising anode material for Li ion batteries.^{54–57}

There have been several previous studies of MoO_2 by X-ray photoelectron spectroscopy.^{2,45,47–49,51,52,58,59} Valence level spectra show that a band of Mo 4d states around 3 eV wide lies above an O 2p band whose width is about 6 eV. However, the energy resolution in this previous work has in general been too poor to properly reveal the expected splitting of the Mo 4d bands predicted by the Goodenough model. The splitting has however been observed in ultraviolet photoemission spectra.^{45,52,58} In addition, XAS has been used to explore the unoccupied O 2p states and has found three distinct peaks 0.4, 3.1, and 4.6 eV above the Fermi energy.⁴⁶ Optical reflectivity measurements have been used to infer that the lowest unfilled Mo 4d levels are situated ~ 2.5 eV above the top of the O 2p bands.^{60–62}

Theoretically MoO_2 has received less attention than MoO_3 , with only a handful of studies in the literature.^{42,46,63–67} These have included tight binding⁴² and cluster calculations.^{42,63–66} Recently, two studies by Eyert and co-workers used LDA within the augmented spherical wave (ASW) method to study the Peierls-like instability in MoO_2 and investigated the Fermi surface of MoO_2 in comparison with angle-resolved photoemission spectroscopy and de Haas–van Alphen measurements.^{46,67} This work identified three Fermi surface sheets with electron effective masses of 0.85 m_0 , 1.87 m_0 , and 2.85 m_0 , where m_0 is the electron rest mass.

In the present study we used GGA density functional theory calculations to study the geometry and electronic structure of MoO_2 and MoO_3 . The theoretical results are compared with high-resolution X-ray photoemission data. We find excellent agreement between experimental X-ray valence band photoemission spectra and the calculated cross-section weighted density of states. At the same time it is shown that the complex core level structure noted previously for MoO_2 and attributed to complex and ill-defined “surface phases” such as Mo_2O_5 ^{47–49,51,52} is intrinsic to the material and arises from final state metallic screening.

2. Theoretical Methods

The periodic DFT code VASP^{68,69} was employed for all our calculations. This uses a plane wave basis set to describe the valence electronic states. The Perdew–Burke–Ernzerhof⁷⁰ (PBE) gradient-corrected functional was used to treat the exchange and correlation. Interactions between the cores (Mo: [Kr] and O: [He]) and the valence electrons were described using the projector-augmented wave⁷¹ (PAW) method.

Structural optimizations of bulk MoO_2 were performed at a series of volumes in order to calculate the equilibrium lattice parameters. In each case the atomic positions, lattice vectors, and cell angles were allowed to relax, while the total volume was held constant. The resulting energy volume curves were fitted to the Murnaghan⁷² equation of state to obtain the equilibrium bulk cell volume. This approach avoids the problems of Pulay stress and changes in basis set which can accompany

volume changes in plane wave calculations. Convergence with respect to k-point sampling and plane wave energy cut off was checked, with a cutoff of 500 eV and a k-point sampling of $4 \times 6 \times 4$ found to be sufficient. Structural optimizations were deemed to be converged when the force on every ion was less than 0.005 eV \AA^{-1} .

As MoO_3 is a layered structure, with the interlayer distance determined by noncovalent interlayer forces, a simple relaxation as outlined above is not sufficient. DFT methods have long been known to be unable to describe van der Waals forces correctly,^{29,73–78} and as expected, attempting to minimize the structure using the system above resulted in the absence of a minimum in the b vector. Indeed, relaxing the stress tensor at an elevated cutoff of 1000 eV gave a b lattice parameter of 16.539 \AA , which far exceeds the experimentally reported value of 13.855 \AA . Thus, we used the method proposed by Coquet and Willock,²⁹ which involved holding the b lattice parameter at the experimental value of 13.855 \AA and optimizing the a and c lattice constants by allowing the atomic coordinates to relax at a series of fixed volumes around the experimentally reported lattice parameters. A cutoff of 500 eV and a k-point sampling of $6 \times 2 \times 6$ were found to be sufficient, and structural optimizations were deemed to be converged when the force on every ion was less than 0.005 eV \AA^{-1} , consistent with the MoO_2 calculations above.

3. Experimental Section

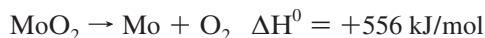
Single-crystal MoO_3 was prepared by a flux method.⁷⁹ The sample selected for study by photoemission had a plate-like morphology with dimensions of around 8 mm \times 4 mm \times 1 mm and came from a batch of crystals previously used in conductivity measurements.⁸⁰ The large flat face had (010) orientation. A second crystal from the batch was ground to a powder, and it was confirmed that the powder X-ray diffraction pattern matched that described in the literature and was consistent with orthorhombic space group $Pbnm$ with $a = 3.962$ \AA , $b = 13.855$ \AA , and $c = 3.696$ \AA .^{4,5,81} MoO_2 was prepared by reduction of MoO_3 in a flowing $\text{H}_2/\text{H}_2\text{O}/\text{Ar}$ mixture as described elsewhere.⁵⁸ The $\text{H}_2/\text{H}_2\text{O}$ atmosphere was set with $p_{\text{H}_2} = 25.8$ Torr, $p_{\text{H}_2\text{O}} = 2.4$ Torr, and with a balance of Ar around 730 Torr, and reduction was carried out at 547 $^\circ\text{C}$ over a period of 4 days. The effective oxygen partial pressure under these conditions is estimated to be about 10^{-11} mbar, and these conditions render MoO_2 the thermodynamically favored product. The O/Mo ratio in the product was established to be 2.000 ± 0.002 by a volumetric procedure involving oxidation by $\text{K}_3\text{Fe}(\text{CN})_6$.⁸² The powder sample was pressed between tungsten carbide dies to give a ceramic disk which was then sintered in vacuo in a sealed quartz tube at 900 $^\circ\text{C}$ to give mechanical strength. The final pelletized sample gave a monoclinic X-ray powder diffraction pattern in agreement with that published previously and consistent with space group $P2_1c$ with $a = 561$ pm, $b = 486$ pm, $c = 563$ pm, and $\beta = 121^\circ$.^{39,42,81}

High-resolution X-ray photoemission spectra were measured in a Scienta ESCA 300 spectrometer. This incorporates a rotating anode Al K α ($h\nu = 1486.6$ eV) X-ray source, a 7-crystal X-ray monochromator, and a 300 mm mean radius spherical sector electron energy analyzer with a parallel electron detection system. The X-ray source was run with 200 mA emission current and 14 kV anode bias, while the analyzer operated at 150 eV pass energy. Gaussian convolution of the analyzer resolution with a line width of 260 meV for the X-ray source gives an effective instrument resolution of 400 meV. Binding energies are referenced to the Fermi energy of a silver sample regularly

TABLE 1: Calculated Lattice Parameters and M–O Bond Distances for Bulk MoO₃ Compared to Previous Theoretical Works and Experiment

	this work	GGA ²⁹	LDA ²⁶	HF ⁷	experiment ⁵	experiment ⁶
<i>a</i>	4.023	4.022	3.729	3.910	3.962	3.963
<i>b</i>	13.855	13.855	13.036	14.271	13.855	13.855
<i>c</i>	3.755	3.752	3.478	3.680	3.699	3.696
<i>d</i> _{M–O1}	1.703	1.70	1.67	1.643	1.710	1.670
<i>d</i> _{M–O2}	1.761	1.75	1.75	1.687	1.958	1.730
<i>d</i> _{M–O2'}	2.278	2.29	2.24	2.237	2.029	2.250
<i>d</i> _{M–O3}	1.975	1.97	1.94	1.937	1.899	1.950
<i>d</i> _{M–O3'}	2.340	2.34	2.32	2.212	2.471	2.250

used to calibrate the spectrometer. Samples were mounted on molybdenum stubs, and in situ cleaning in the spectrometer was achieved by electron beam heating of the rear of the stub in the sample preparation chamber. The heater was configured to eliminate direct impact of electrons on the front of the sample. This cleaning heating arrangement has been used in many previous studies in the Scienta XPS system.^{83–87} The surface of as-presented MoO₂ was contaminated with MoO₃ (see below) formed when the reduced sample is exposed to air. Simple thermochemical considerations suggest that it should be possible to find a temperature regime where MoO₃ will be unstable with respect to decomposition into MoO₂ without the MoO₂ itself decomposing to give Mo metal because the enthalpy change is lower for the former process:



It was established empirically that heating at around 500 °C for 1 h led to removal of MoO₃ contamination. This temperature is somewhat lower than that used in the bulk synthesis because the oxygen partial pressure in the spectrometer UHV system is below 10^{−12} mbar and is therefore lower than that established by the H₂/H₂O mixture.

The core lines were fitted using a series of pseudo-Voigt functions with a variable Gaussian to Lorentzian ratio. In the initial stages of the curve fitting the data for MoO₂ the separation between the chemically shifted components of the Mo 3d spin–orbit doublets was constrained at the value found for MoO₃, where a single pair of spin–orbit split components dominates the spectrum. In addition, the intensity ratio between 3d_{5/2} and 3d_{3/2} components was fixed at 6:4. However, in the later stages of the curve fit this latter constraint was relaxed to allow for the possibility that the 3d_{5/2} and 3d_{3/2} spin orbitals may have different ionization cross sections. In curve fitting the data for MoO₂ it was further necessary to allow the screened final state components (see below) of the Mo 3d core line to assume the asymmetric line shape characteristic of metallic materials due to electron hole pair excitations around the Fermi energy.

4. Results and Discussion

Computational Results on MoO₃. The GGA-calculated lattice parameters for MoO₃ are shown in Table 1. Calculated lattice constants are in excellent agreement with experiment^{5,6} and with previous GGA calculations.²⁹ GGA is known to overestimate lattice vectors, whereas LDA underestimates lattice constants, a trend which is clear from Table 1. The calculated

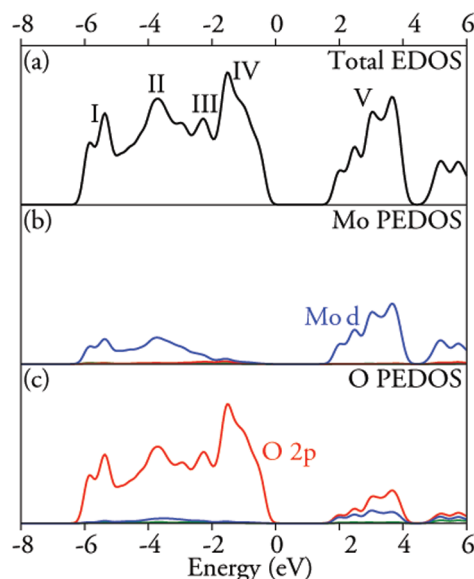


Figure 3. Electronic density of states for MoO₃: (a) Total EDOS, (b) Mo PEDOS, and (c) O PEDOS. The blue lines represent *d* states, green *s* states, and red *p* states. The highest occupied state is set to 0 eV.

bond lengths are also in agreement with previous GGA calculations²⁹ but are on average much closer to the experimental results of Kihlberg⁶ than to the study of Sitepu et al.,⁵ even though the starting structure used for the minimization was taken from the latter. Both studies reported that MoO₃ crystallizes with space group *Pbnm*. From analysis of our geometries, we conclude that the structure derived by Kihlberg et al. would seem more consistent with our calculated structure than that of Sitepu et al.

The GGA-calculated total and partial (ion decomposed) electronic densities of states EDOS/PEDOS for MoO₃ is shown in Figure 3. The valence band is split up into four main regions (labeled I–IV), with the conduction band labeled V. Region I is dominated by O 2p states with some significant mixing with Mo 4d states. Region II is mainly composed of O 2p states, again with some mixing with the Mo 4d states. Region III is made up of mainly O 2p states, with some small contributions from Mo 4d, and region IV is completely dominated by O 2p states, with only a very minor contribution from any Mo states. The conduction band is dominated by Mo *d* states with some hybridization with O 2p states. Valence bands with O 2p states dominating at the VBM and cation *d* states dominating at the CBM are a general feature of the electronic structure of wide band gap binary d⁰ oxides.^{33,73} Above the Fermi level, the two oxygen peaks found at ~1.4, ~2.2, and ~3.05 eV and are consistent with previous XAS results, which found peaks at 1.4 and 3.1 eV above the Fermi energy.²⁴

The calculated band structure for MoO₃ along the high-symmetry points is shown in Figure 4. The VBM is found to be situated at U, with the CBM situated at Γ , resulting in an indirect band gap of 1.95 eV. The lowest direct gap is found at Γ and has a value of 2.76 eV. Previous calculations using HF⁷ and LAPW within the LDA framework²⁸ placed the VBM at R, which in our study is 0.03 eV below U. The indirect nature of the lowest gap accounts for the discrepancy between the positions of absorption edges for thin film and single-crystal samples alluded to above. However, as is usual with density functional calculations the magnitude of the lowest gap derived from the calculation is smaller than that observed experimentally.

Computational Results on MoO₂. Table 2 displays the GGA-calculated structural data for MoO₂. The calculated lattice

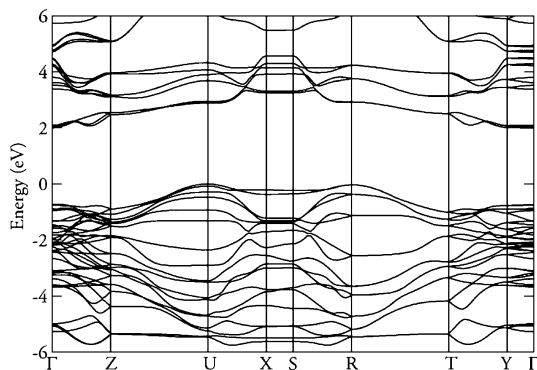


Figure 4. Electronic band structure along the high-symmetry points for MoO₃. The highest occupied state is set to 0 eV.

TABLE 2: Calculated Lattice Parameters and M–O and Mo–Mo Interatomic Distances for Bulk MoO₂ Compared to Experiment

	this work	experiment ⁴⁰
<i>a</i>	5.615	5.611
<i>b</i>	4.924	4.856
<i>c</i>	5.692	5.628
<i>d</i> _{Mo–O(a)}	2.088	2.065
<i>d</i> _{Mo–O(a)} '	2.090	2.073
<i>d</i> _{Mo–O(a)} ''	2.005	1.977
<i>d</i> _{Mo–O(b)}	2.012	1.995
<i>d</i> _{Mo–O(b)} '	1.995	1.972
<i>d</i> _{Mo–O(b)} ''	2.000	1.984
<i>d</i> _{Mo–Mo}	2.492, 3.126	2.510, 3.020

parameters and bond lengths are in generally good agreement with experimental data⁴⁰ save for the small overestimates compared to experiment to be expected from GGA calculations. Although there have been two previous calculations on monoclinic MoO₂, they neglected to report any structural data, so comparison with this earlier result is not possible (Table 2).^{46,67}

Figure 5a–c shows the EDOS/PEDOS for MoO₂. The EDOS can be split up into five main regions, labeled I–V in Figure 3a. Region I spans from –8 to –6 eV and is mainly composed of O 2p states with some significant mixing with Mo d states. Between –6 and –2 eV (region II), O 2p states dominate, with some hybridization with Mo d states. Regions III and IV

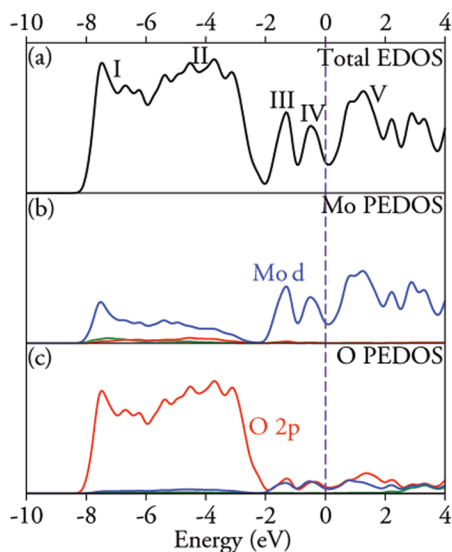


Figure 5. Electronic density of states for MoO₂: (a) Total EDOS, (b) Mo PEDOS, and (c) O PEDOS. The blue lines represent *d* states, green *s* states, and red *p* states. The dashed line denotes the Fermi energy.

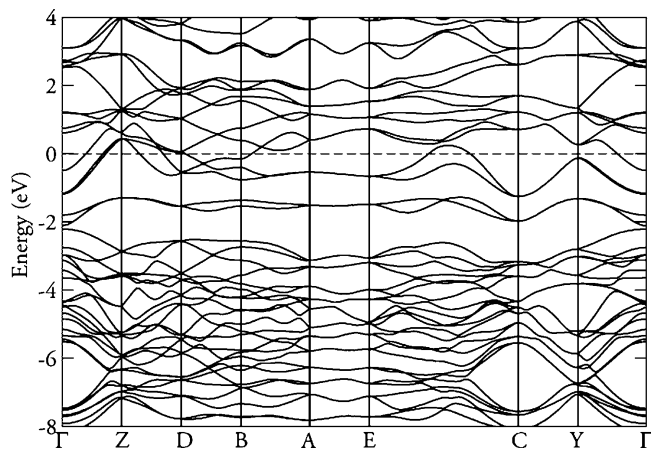


Figure 6. Electronic band structure along the high-symmetry points for MoO₂. The dashed line denotes the Fermi energy.

(between –2 eV and the Fermi level) are dominated by Mo *d* states, with peaks at ~–1.35 and ~–0.5 eV. Above the Fermi level, the Mo 4*d* states again dominate, with distinct peaks at ~1.27 and 2.20 eV.

The calculated band structure for MoO₂ is shown in Figure 6. Referring to the PEDOS, one can clearly see the O 2*p* bands between ~–8 and –2 eV, with the Mo 4*d* states spanning from –2 to +4 eV. Our band structure is in excellent agreement with that of Eyert^{46,67} and co-workers. Of particular note is that there are two Mo 4*d* bands which lie below the Fermi energy across all of the Brillouin zone. These correspond to the split-off bonding *t*_{1i} states of the Goodenough model. Two further Mo 4*d* bands lie below the Fermi energy along Γ –Y–C and E–A–B–D directions but push through the Fermi level along Γ –Z, Z–D, and C–E. These crossings are responsible for the metallic nature of MoO₂.

Core Level Photoemission Spectra of MoO₃ and MoO₂.

Core XPS data are shown in Figures 7–9, whilst the parameters derived from curve fits to the core lines are given in Table 3. The surface of untreated MoO₃ showed a high level of carbon contamination. The sample was therefore annealed in situ in the spectrometer UHV system by heating to 300 °C. This annealing condition represented a best compromise in terms of removal of excessive surface C contamination without pronounced reduction of the surface and led to a C 1*s*/O 1*s* intensity ratio of 0.04. The O/Mo atomic ratio derived by correction of O 1*s* and Mo 3*d* intensities by atomic sensitivity factors⁸⁸ was 3.2, in good agreement with the nominal value of 3.0, especially bearing in mind that the single-crystal surface is probably terminated with an O layer. The Mo 3*d* core level spectrum of the annealed MoO₃ is dominated by a spin–orbit doublet with peaks at binding energies 232.38 ± 0.10 and 235.53 ± 0.10 eV. This is associated with Mo in the formal (VI) oxidation state. In addition, a weak doublet shifted to low binding energy by 1.60 eV was observed in the Mo 3*d* core level spectrum, as shown in Figure 7. This indicates that there is very slight surface reduction. The Mo 3*d* core level spectrum of the as-presented MoO₂ was much more complex and appeared to consist of a superposition of structure intrinsic to MoO₂ along with a spin–orbit doublet associated with MoO₃ surface contamination (Figure 7). The MoO₂ sample was therefore heated in situ to 500 °C for 1 h by electron beam heating as described in the Experimental Section. This treatment reduced the C 1*s*/O 1*s* intensity ratio to below 0.01 and gave a surface with an apparent O/Mo ratio as defined above equal to 2.1, again in good agreement with the nominal value of 2.0. The annealing

TABLE 3: Parameters from Curve Fits to O 1s and Mo 3d Core Lines of MoO₃ and MoO₂

material	peak ^a	binding energy (eV)	fwhm (eV)	relative area
MoO ₃	O 1s main	530.31	1.17	1.00
cleaned	<i>O 1s contaminant</i>	531.46	1.37	0.09
MoO ₂	O 1s main	530.11	1.18	1.00
as presented	<i>O 1s contaminant</i>	531.27	1.51	0.40
MoO ₂	O 1s main	530.05	1.01	1.00
cleaned	O 1s satellite	531.17	1.82	0.63
MoO ₃	Mo 3d _{5/2} 4d ⁰	232.48	0.86	1.00
cleaned	Mo 3d _{3/2} 4d ⁰	235.63	0.92	0.65
	<i>Mo 3d_{5/2} 4dⁿ</i>	230.75	0.74	0.03
	<i>Mo 3d_{3/2} 4dⁿ</i>	233.90	0.83	0.02
MoO ₂	Mo 3d _{5/2} screened	229.27	0.60 (0.26/0.34) ^b	1.00
cleaned				
	Mo 3d _{3/2} screened	232.47	0.75 (0.33/0.42) ^b	0.67
	Mo 3d _{5/2} unscreened	231.00	2.14	1.25
	Mo 3d _{3/2} unscreened	234.21	2.21	0.83
	<i>Mo 3d_{5/2} metal</i>	228.29	0.88	0.005
	<i>Mo 3d_{3/2} metal</i>	231.49	0.90	0.003

^a Entries in italics relate to structure associated with surface contamination (MoO₃ and as-presented MoO₂) or Mo metal (formed in electron beam heating of MoO₂). ^b Screened final state peaks for MoO₂ are asymmetric. The numbers in parentheses give the widths at half-maximum height about the midline of the peak.

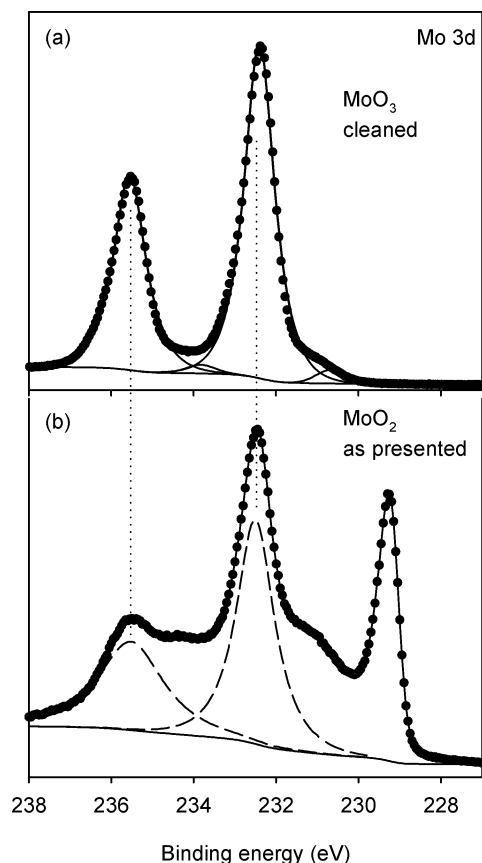


Figure 7. (a) Mo 3d structure of single-crystal MoO₃ after gentle anneal in UHV. There is evidence of slight surface reduction. (b) Mo 3d structure of as-presented MoO₂. The spectrum is a superposition of intrinsic structure associated with MoO₂ (see Figure 8a) along with a contribution from surface MoO₃ contamination. The MoO₃ contribution is indicated by the dashed lines.

treatment also led to removal of structure in the Mo 3d region associated with MoO₃ to leave a spectrum dominated by two overlapping spin–orbit doublets, as shown in Figure 8. The

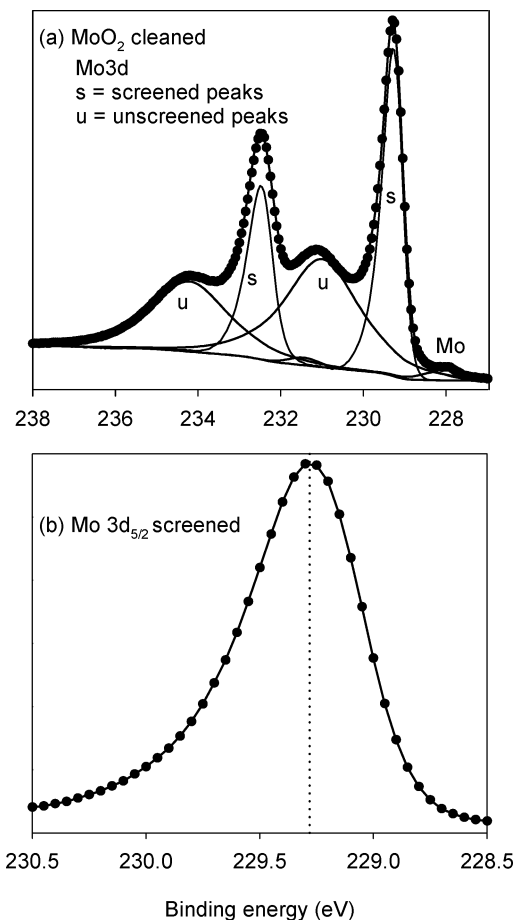


Figure 8. (a) Mo 3d structure of MoO₂ after UHV electron beam anneal at 500 °C for 1 h. Structure due to MoO₃ has been removed to reveal an intrinsic spectrum consisting of two overlapping spin–orbit doublets. There is also a very weak doublet associated with Mo metal produced around the edge of the sample by stray electrons from the electron beam heater. However, this structure contributes only around 0.2% of the intensity of the overall spectrum. (b) Expanded view of the Mo 3d_{5/2} screened final state component after stripping out other components generated by the peak fit above. This reveals the asymmetric line shape of the screened final state component.

resolution achieved in the current work is much better than in previous experimental work on MoO₂.^{2,47–49,51,52,58,59} The complex core line shape is characteristic of narrow band metallic oxides where the width of the conduction band is comparable with the potential generated by the core hole.^{89–954–10} The core hole therefore pulls a localized 4d level out of the conduction band. As discussed in detail elsewhere^{89,91–94} the components at low binding energy (labeled (s) in Figure 8) are due to well-screened final states in which the localized level becomes occupied by an itinerant conduction electron, while the broader components at higher binding energy are associated with unscreened final states, labeled (u) in the figure, where the localized level remains empty. The high resolution achieved in the current work allows us to measure the full width at half-maximum height (fwhm) of the 3d_{5/2} screened final state peak as 0.60 eV. The peaks associated with screened final states display a distinctly asymmetric line shape resulting from electron–hole pair excitations around the Fermi energy induced by the appearance of the core hole. The higher binding energy unscreened 3d_{5/2} peak has a fwhm of 2.14 eV, and in an unconstrained curve fit using pseudo-Voigt functions the peak is found to have 80% Lorentzian character. This is associated with lifetime broadening characteristic of the final state screening

process. The energy separation between screened and unscreened $3d_{5/2}$ peaks is 1.63 eV, which is almost exactly equal to the plasmon energy of 1.56 eV for MoO_2 ⁴⁵ measured by electron energy loss spectroscopy. The unscreened final state peaks may therefore be regarded as unusually strong plasmon satellites, as first proposed by Wertheim.⁹² Our interpretation of the core level structure in terms of intrinsic final state screening effects is very different to that popular in the catalytic literature, which has mostly ignored the narrow band metallic nature of MoO_2 and attempted to associate what we believe to be intrinsic satellites with “ Mo_2O_3 ” surface contamination^{47–49,51,52} even though there is no known Mo(V) oxide bulk phase. We note here that Chambers and co-workers studied the photoelectron diffraction profiles of satellites found in Ru 3d core XPS of metallic RuO_2 .⁹⁶ The satellites were very similar to those observed in the current work, and it was shown that the angular variation in the satellite intensity mirrored that of the main peak. This establishes definitively that the satellite intensity derives from Ru ions occupying identical sites to those responsible for the main peak and that the satellite structure is therefore intrinsic to RuO_2 and does not arise from ill-defined surface phases with oxidation states greater than (IV).

Further support for our interpretation is provided by the fact that the O 1s spectrum of MoO_2 also contains a very strong satellite separated from the main peak by 1.12 eV, as shown in Figure 9. This is a little lower than the satellite energy for the Mo 3d core lines, but it is not unreasonable to expect that the screening response upon generation of an O 1s core hole should be different than that in response to generation of a Mo 3d core hole because the conduction band is composed mainly of Mo 4d states. We can rule out the possibility that the O 1s satellite arises from OH or carbonate surface contamination (which can give peaks to high binding energy of the main peak in oxides) on the basis that (i) the satellite is much more intense than the contaminant high binding energy structure found for MoO_3 , even though the latter has been subject to in situ surface cleaning at a lower temperature than MoO_2 , (ii) the satellite intensity for MoO_2 increases after in situ cleaning (this is compatible with removal of a surface layer of MoO_3 , which does not have a strong satellite, but difficult to understand if the satellite is associated with surface contamination), (iii) the satellite peak has a dominantly Lorentzian line shape (80% Lorentzian contribution to the pseudo-Voigt profile in an unconstrained fit) as expected for a plasmon loss peak, (iv) similar O 1s structure is found for other metallic oxides, such as the sodium tungsten bronzes,⁹² Sb-doped SnO_2 ,⁹⁷ and defect doped PbO_{2-x} .⁹⁸ The closely related nonmetallic oxides WO_3 , undoped SnO_2 , and PbO do not display a pronounced O 1s satellite.

Valence Band Spectra. Valence band X-ray photoemission spectra of MoO_3 and MoO_2 are shown in Figure 10. The spectra may be compared with the computed density of states but with the different partial densities of states weighted by one-electron ionization cross sections. At $h\nu = 1486.6$ eV, the relevant one-electron cross section for ionization of O 2p states is 0.06 kB, whereas the cross section for Mo 4d states is 0.92 kB. The cross-section weighted density of states is therefore very much dominated by the Mo 4d contribution which is weighted by a factor of 15 relative to O 2p.⁹⁹

For MoO_3 the biggest Mo 4d contribution to the occupied density of states is found in regions I and II toward the middle and bottom of the valence band (see Figure 10), with only a small contribution in region IV where the O 2p partial density of states is at a maximum. In agreement with the calculation the structure associated with III and IV appears as a shoulder

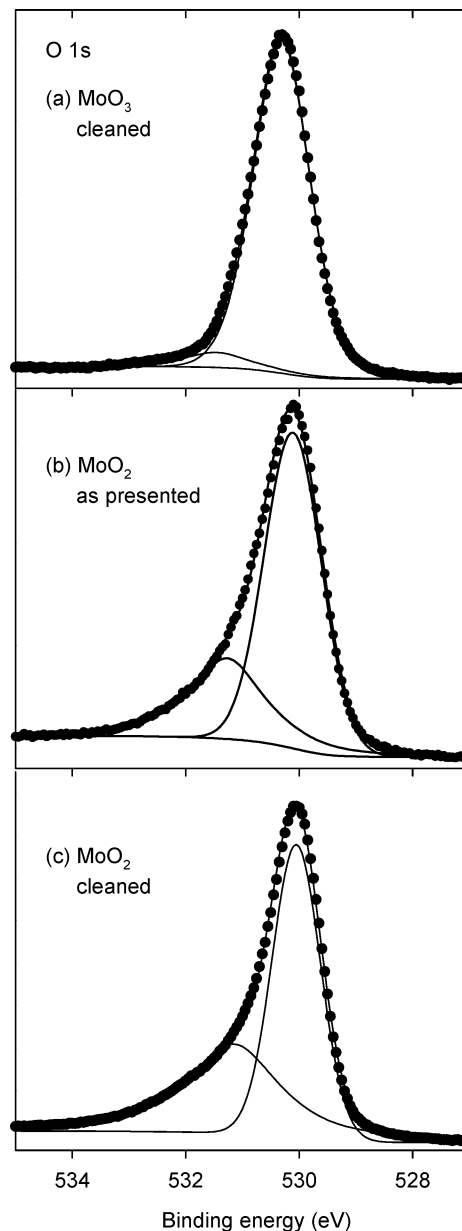


Figure 9. (a) O 1s core level structure of MoO_3 after cleaning samples in UHV at 300 °C. (b) O 1s core line of as-presented MoO_2 . (c) O 1s core line of MoO_2 after in situ cleaning. Note that the intensity of the high binding energy satellite peak of MoO_2 increases after the cleaning procedure.

on the low binding energy side of II in the experimental spectrum rather than IV appearing as a maximum, as in the unweighted density of states. This situation is reversed in lower energy ultraviolet photoemission spectra where peak IV dominates the valence band photoemission.²³ In agreement with the core level data a weak peak associated with occupied Mo 4d states appears close to the Fermi energy. This must be associated with O vacancy defects to give MoO_{3-x} , which is no longer $4d^0$.²³ Linear extrapolation of the valence band edge to zero intensity gives a valence band onset energy of 2.8 eV. If it is assumed that the defect states pin the Fermi energy close to the bottom of the conduction band this onset energy is in agreement with an indirect gap of 2.82 eV as determined by absorption measurements on single crystals.¹⁰ The width of the valence band is calculated to be ~ 6.3 eV, which is just under the value of 7 eV measured in the present work and in ref 23. The small

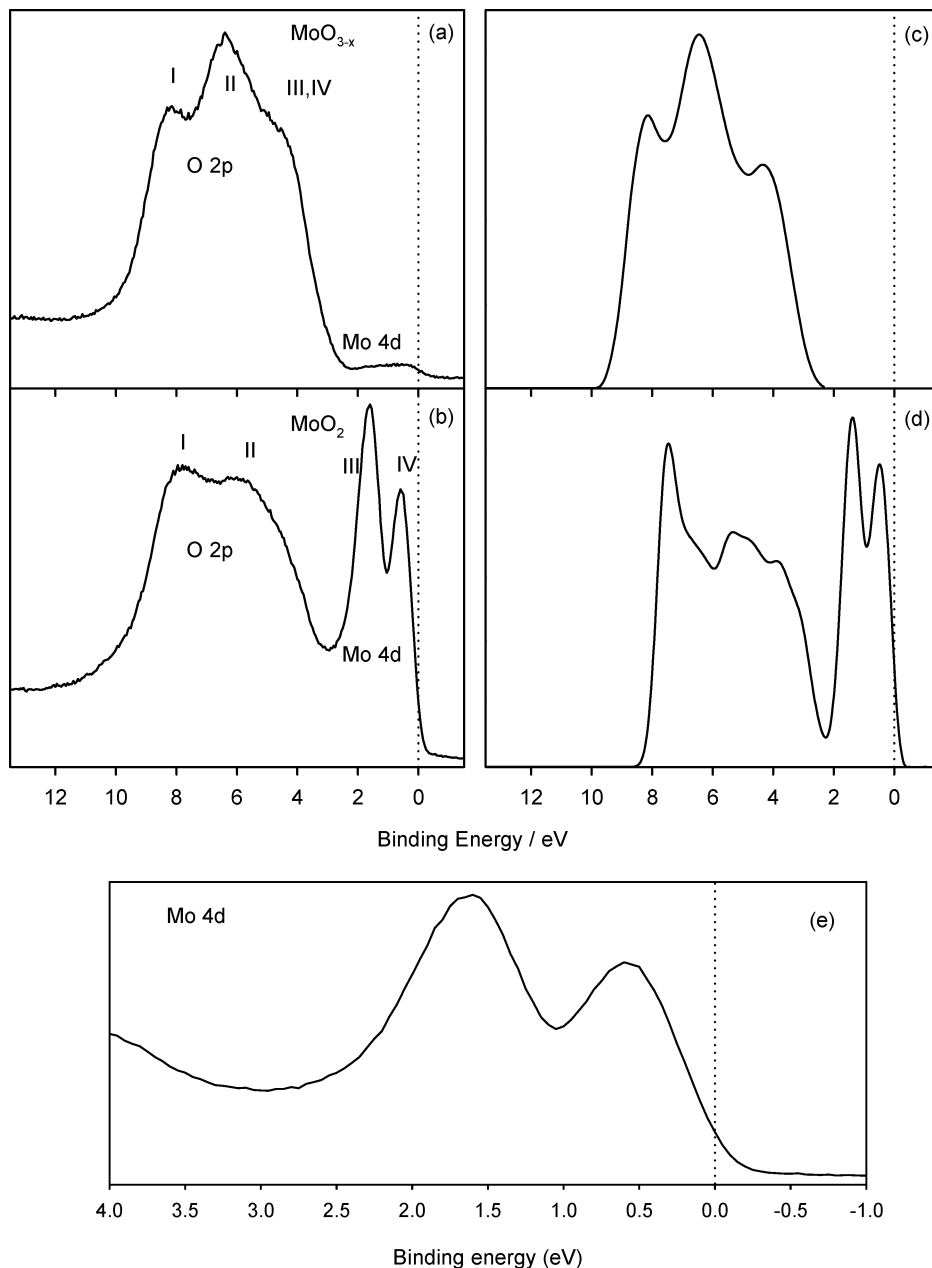


Figure 10. Valence band XPS of (a) MoO₃ and (b) MoO₂. The spectrum of MoO₃ contains some weak Mo 4d states in the bulk band gap which must be associated with partial surface reduction. The strong Mo 4d structure for MoO₂ is split into two due to Mo–Mo bonding along the *c* axis of the distorted rutile structure. (c and d) Computed cross-section weighted densities of states. (e) Detail of the Mo 4d conduction band structure for MoO₂.

discrepancy is not surprising as GGA calculations are known to slightly underestimate the width of valence bands.^{83,100–102}

The photoemission spectrum of MoO₂ also mirrors the Mo 4d partial density of states. Two strong and relatively narrow peaks appear above the O 2p valence band as in the calculation. These are associated with the σ - and π -bonding states discussed above: in agreement with the calculation the π bonding is not strong enough to split the $t_{1\perp}$ (π) bands off completely from the rest of the unoccupied Mo 4d bands to give an insulating material. Thus, MoO₂ is a metallic oxide, as is found in transport measurements. However, the Fermi level is located in a pronounced trough in the density of states. This is in agreement with the placement of the Fermi level relative to the peak maximum of IV shown in greater detail in the lower panel of Figure 10. The peaks in the Mo 4d bands are found 0.60 and 1.60 eV below the Fermi level, in good agreement with the computed values of 0.50 and 1.35 eV, respectively. The overall

width of the occupied band states is just under 10 eV, which is again slightly greater than the calculated value of 8 eV.

5. Conclusion

The geometry and electronic structure of MoO₃ and MoO₂ have been studied using high-resolution X-ray photoemission spectroscopy and ab initio density functional theory calculations. We find good agreement between the calculated structural data and previous X-ray diffraction data. Cross-section weighted GGA density of states and the XPS spectra are in excellent agreement, with MoO₃ shown to be insulating and MoO₂ shown to be metallic, consistent with previous experimental studies. The position of the Fermi level for MoO₂ is, however, found to reside in a deep trough in the density of states. It is demonstrated that satellite peaks found in core photoemission spectra of MoO₂ derive from final state screening effects, and the separation

between the “main” peaks and their satellites is very close to the conduction electron plasmon energy measured in electron energy loss spectroscopy.

Acknowledgment. The theoretical work was supported by Science Foundation Ireland through the research frontiers programme (grant nos. 08/RFP/MTR1044 and 09/RFP/MTR2274). Calculations were performed on the IITAC supercomputer as maintained by TCHPC and the Stokes supercomputer as maintained by ICHEC. The NCESS facility at Daresbury Laboratory is supported by EPSRC grant EP/E025722/1. D.J.P. is supported by a Junior Research Fellowship at Christchurch College, Oxford.

References and Notes

- Hamnett, A.; Goodenough, J. B.; *Landolt-Bornstein Numerical Data and Functional Relationships in Science and Technology*; Springer-Verlag: Berlin, 1984; Vol. 17g, Part III.
- Khyzhun, O. Y.; Bekenev, V. L.; Solonin, Y. M. *J. Alloys Compd.* **2008**, *459*, 22.
- Carcia, P. F.; McCarron, E. M. *Thin Solid Films* **1987**, *155*, 53.
- Andersson, G.; Magneli, A. *Acta Chem. Scand.* **1950**, *4*, 793.
- Sitepu, H.; O'Connor, B. H.; Li, D. *J. Appl. Crystallogr.* **2005**, *38*, 158.
- Kihlberg, L. *Ark. Kem.* **1964**, *21*, 443.
- Cora, F.; Patel, A.; Harrison, N. M.; Roetti, C.; Catlow, C. R. A. *J. Mater. Chem.* **1997**, *7*, 959.
- Sabhpathi, V. K.; Hussain, O. M.; Uthanna, S.; Naidu, B. S.; Reddy, P. J. *J. Mater. Sci. Lett.* **1995**, *14*, 411.
- Sabhpathi, V. K.; Hussain, O. M.; Uthanna, S.; Reddy, P. J. *Mater. Lett.* **1994**, *20*, 175.
- Juryska, R. *Phys. Stat. Solidi B: Basic Res.* **1975**, *72*, K161.
- Kung, H. K. *Transition metal oxides: surface chemistry and catalysis*; Elsevier: Amsterdam, 1989; Vol. 45.
- Haber, J.; Wojciechowska, M. MgF₂: Supported transition metal oxide monolayers-A novel type of catalysts. 2nd Tokyo Conference on Advanced Catalytic Science and Technology, Tokyo, Japan 1994.
- Kim, M. C.; Kim, K. L. *Korean J. Chem. Eng.* **1996**, *13*, 1.
- Grunert, W.; Stakheev, A. Y.; Feldhaus, R.; Anders, K.; Shpiro, E. S.; Minachev, K. M. *J. Catal.* **1992**, *135*, 287.
- Grunert, W.; Stakheev, A. Y.; Morke, W.; Feldhaus, R.; Anders, K.; Shpiro, E. S.; Minachev, K. M. *J. Catal.* **1992**, *135*, 269.
- Matralis, H.; Theret, S.; Bastians, P.; Ruwet, M.; Grange, P. *Appl. Catal., B* **1995**, *5*, 271.
- Taylor, S. H.; Hargreaves, J. S. J.; Hutchings, G. J.; Joyner, R. W. *Appl. Catal., A* **1995**, *126*, 287.
- Ozkan, U. S.; Gooding, R. E.; Schilf, B. T. *Partial oxidation of C-5 hydrocarbons to maleic and phthalic anhydrides over molybdate-based catalysts*; Symposium on Catalytic Heterogeneous Hydrocarbon Oxidation, 211th National Meeting of the American Chemical Society, New Orleans, LA, 1996.
- Li, Y. M.; Kudo, T. *Properties of mixed-oxide MoO₃/V₂O₅ electrochromic films coated from peroxo-polymolybdovanadate solutions*; 1st International Meeting on Electrochromism (IME-1), Murano Venice, Italy, 1994.
- Yao, J. N.; Hashimoto, K.; Fujishima, A. *Nature* **1992**, *355*, 624.
- Sheehan, P. E.; Lieber, C. M. *Science* **1996**, *272*, 1158.
- Lee, S. H.; Kim, Y. H.; Deshpande, R.; Parilla, P. A.; Whitney, E.; Gillaspie, D. T.; Jones, K. M.; Mahan, A. H.; Zhang, S. B.; Dillon, A. C. *Adv. Mater.* **2008**, *20*, 3627.
- Firment, L. E.; Ferretti, A. *Surf. Sci.* **1983**, *129*, 155.
- Learmonth, T.; McGuinness, C.; Glans, P. A.; Kennedy, B.; John, J. S.; Guo, J. H.; Greenblatt, M.; Smith, K. E. *Phys. Rev. B* **2009**, *79*, 8.
- Tokarz-Sobieraj, R.; Hermann, K.; Witko, M.; Blume, A.; Mestl, G.; Schlögl, R. *Surf. Sci.* **2001**, *489*, 107.
- Chen, M.; Waghmare, U. V.; Friend, C. M.; Kaxiras, E. *J. Chem. Phys.* **1998**, *109*, 6854.
- Rozzi, C. A.; Manghi, F.; Parmigiani, F. *Phys. Rev. B* **2003**, *68*, 075106.
- Sayed, A. D.; Amriou, T.; Pernisek, M.; Khelifa, B.; Mathieu, C. *Chem. Phys.* **2005**, *316*, 72.
- Coquet, R.; Willock, D. J. *Phys. Chem. Chem. Phys.* **2005**, *7*, 3819.
- Chen, M.; Friend, C. M.; Kaxiras, E. *J. Chem. Phys.* **2000**, *112*, 9617.
- Chen, M.; Friend, C. M.; Kaxiras, E. *J. Am. Chem. Soc.* **2001**, *123*, 2224.
- Scanlon, D. O.; Walsh, A.; Morgan, B. J.; Nolan, M.; Fearon, J.; Watson, G. W. *J. Phys. Chem. C* **2007**, *111*, 7971.
- Morgan, B. J.; Watson, G. W. *Surf. Sci.* **2007**, *601*, 5034.
- Nolan, M.; Parker, S. C.; Watson, G. W. *Surf. Sci.* **2005**, *595*, 223.
- Nolan, M.; Watson, G. W. *J. Chem. Phys.* **2006**, *125*, 144701.
- Walsh, A.; Yan, Y. F.; Al-Jassim, M. M.; Wei, S. H. *J. Phys. Chem. C* **2008**, *112*, 12044.
- Magneli, A.; Blomberg, B.; Kihlberg, L.; Sundkvist, G. *Acta Chem. Scand.* **1955**, *9*, 1382.
- Heinrich, V. E.; Cox, P. A. *The Surface Science of Metal Oxides*; Cambridge University Press: Cambridge, 1994.
- Magneli, A.; Andersson, G. *Acta Chem. Scand.* **1955**, *9*, 1378.
- Brandt, B. G. *Acta Chem. Scand.* **1967**, *21*, 661.
- Camargo, A. C.; Igualada, J. A.; Beltran, A.; Llusar, R.; Longo, E.; Andres, J. *Chem. Phys.* **1996**, *212*, 381.
- Rogers, D. B.; Shannon, R. D.; Sleight, A. W.; Gillson, J. L. *Inorg. Chem.* **1969**, *8*, 841.
- Cheetham, A. K.; Rao, C. N. R. *Acta Crystallogr., Sect. B: Struct. Sci.* **1976**, *32*, 1579.
- Goodenough, J. B. *Prog. Solid State Chem.* **1971**, *5*, 145.
- Gulino, A.; Parker, S.; Jones, F. H.; Egdel, R. G. *J. Chem. Soc., Faraday Trans.* **1996**, *92*, 2137.
- Eyert, V.; Horny, R.; Hock, K. H.; Horn, S. *J. Phys.-Condes. Matter* **2000**, *12*, 4923.
- Katrib, A.; Leflaive, P.; Hilaire, L.; Maire, G. *Catal. Lett.* **1996**, *38*, 95.
- Katrib, A.; Logie, V.; Peter, M.; Wehrer, P.; Hilaire, L.; Maire, G. *J. Chim. Phys. Phys.-Chim. Biol.* **1997**, *94*, 1923.
- Katrib, A.; Logie, V.; Saurel, N.; Wehrer, P.; Hilaire, L.; Maire, G. *Surf. Sci.* **1997**, *377–379*, 754.
- Katrib, A.; Mey, D.; Maire, G. *Catal. Today* **2001**, *179*.
- Katrib, A.; Sobczak, J. W.; Krawczyk, M.; Zommer, L.; Benadda, A.; Jablonski, A.; Maire, G. *Surf. Interface Anal.* **2002**, *34*, 225.
- Marin-Flores, O.; Scudiero, L.; Ha, S. *Surf. Sci.* **2009**, *603*, 2327.
- de Moraes, M. A. B.; Trasferetti, B. C.; Rouxinol, F. P.; Landers, R.; Durrant, S. F.; Scarminio, J.; Urbano, A. *Chem. Mater.* **2004**, *16*, 513.
- Auborn, J. J.; Barberio, Y. L. *J. Electrochem. Soc.* **1987**, *134*, 638.
- Liang, Y. G.; Yang, S. J.; Yi, Z. H.; Lei, X. F.; Sun, J. T.; Zhou, Y. H. *Mater. Sci. Eng. B: Solid State Mater. Adv. Technol.* **2005**, *121*, 152.
- Yang, L. C.; Gao, Q. S.; Zhang, Y. H.; Tang, Y.; Wu, Y. P. *Electrochem. Commun.* **2008**, *10*, 118.
- Yang, L. C.; Gao, Q. S.; Tang, Y.; Wu, Y. P.; Holze, R. *J. Power Sources* **2008**, *179*, 357.
- Beatham, N.; Orchard, A. F. *J. Electron Spectrosc. Relat. Phenom.* **1979**, *16*, 77.
- Werfel, F.; Minni, E. *J. Phys. C: Solid State Phys.* **1983**, *16*, 6091.
- Chase, L. L. *Phys. Rev. B* **1974**, *10*, 2226.
- Chase, L. L. *Bull. Am. Phys. Soc.* **1974**, *19*, 271.
- Dissanayake, M.; Chase, L. L. *Phys. Rev. B* **1978**, *18*, 6872.
- Burdett, J. K. *Inorg. Chem.* **1985**, *24*, 2244.
- Sasaki, T. A.; Kiuchi, K. *Chem. Phys. Lett.* **1981**, *84*, 356.
- Sasaki, T. A.; Soga, T.; Adachi, H. *Phys. Stat. Solidi B: Basic Res.* **1982**, *113*, 647.
- Yoshino, H.; Shimokoshi, K.; Miyazaki, E. *J. Electron Spectrosc. Relat. Phenom.* **1985**, *36*, 269.
- Moosburger-Will, J.; Kuendel, J.; Klemm, M.; Horn, S.; Hofmann, P.; Schwingenschloegl, U.; Eyert, V. arXiv 2009, arXiv:0812.1911.
- Kresse, G.; Furthmüller, J. *Comput. Mater. Sci.* **1996**, *6*, 15.
- Kresse, G.; Hafner, J. *Phys. Rev. B* **1994**, *49*, 14251.
- Perdew, J. P.; Burke, K.; Ernzerhof, M. *Phys. Rev. Lett.* **1997**, *78*, 1396.
- Bloch, P. E. *Phys. Rev. B* **1994**, *50*, 17953.
- Murnaghan, F. D. *Proc. Natl. Acad. Sci. U.S.A.* **1944**, *30*, 244.
- Scanlon, D. O.; Walsh, A.; Morgan, B. J.; Watson, G. W. *J. Phys. Chem. C* **2008**, *112*, 9903.
- Walsh, A.; Watson, G. W. *J. Solid State Chem.* **2005**, *178*, 1422.
- Walsh, A.; Watson, G. W. *Phys. Rev. B* **2004**, *70*, 235114.
- Watson, G. W. *J. Chem. Phys.* **2001**, *114*, 758.
- Rydberg, H.; Dion, M.; Jacobson, N.; Schroder, E.; Hyldgaard, P.; Simak, S. I.; Langreth, D. C.; Lundqvist, B. I. *Phys. Rev. Lett.* **2003**, *91*, 126402.
- Kerber, T.; Sierka, M.; Sauer, J. *J. Comput. Chem.* **2008**, *29*, 2088.
- Wanklyn, B. M. *J. Mater. Sci.* **1972**, *7*, 813.
- Pandit, A. K.; Prasad, M.; Ansari, T. H.; Singh, R. A.; Wanklyn, B. M. *Solid State Commun.* **1991**, *80*, 125.
- Magneli, A.; Andersson, G.; Blomberg, B.; Kihlberg, L. *Anal. Chem.* **1952**, *24*, 1998.
- Choain, C.; Marion, F. *Bull. Soc. Chim. Fr.* **1963**, 212.
- Arnold, T.; Payne, D. J.; Bourlange, A.; Hu, J. P.; Egdel, R. G.; Piper, L. F. J.; Colakerol, L.; De Masi, A.; Glans, P.-A.; Learmonth, T.; Smith, K. E.; Guo, J.; Scanlon, D. O.; Walsh, A.; Morgan, B. J.; Watson, G. W. *Phys. Rev. B* **2009**, *79*, 075102.
- Payne, D. J.; Egdel, R. G.; Walsh, A.; Watson, G. W.; Guo, J.; Glans, P. A.; Learmonth, T.; Smith, K. E. *Phys. Rev. Lett.* **2006**, *96*, 157403.

- (85) Lynch, C. C. B.; Egdell, R. G.; Law, D. S. L. *Chem. Phys. Lett.* **2005**, *401*, 223.
- (86) Morris, D.; Dou, Y.; Rebane, J.; Mitchell, C. E. J.; Egdell, R. G.; Law, D. S. L.; Vittadini, A.; Casarin, M. *Phys. Rev. B* **2000**, *61*, 13445.
- (87) Hu, J. P.; Payne, D. J.; Egdell, R. G.; Glans, P. A.; Learmonth, T.; Smith, K. E.; Guo, J.; Harrison, N. M. *Phys. Rev. B* **2008**, *77*, 155115.
- (88) In *Practical Surface Analysis*; Briggs, D., Seah, M. P., Eds.; John Wiley: Chichester, 1994.
- (89) Beatham, N.; Cox, P. A.; Egdell, R. G.; Orchard, A. F. *Chem. Phys. Lett.* **1980**, *69*, 479.
- (90) Kotani, A.; Toyozawa, Y. *J. Phys. Soc. Jpn.* **1974**, *37*, 912.
- (91) Campagna, M.; Wertheim, G. K.; Shanks, H. R.; Zumsteg, F.; Banks, E. *Phys. Rev. Lett.* **1975**, *34*, 738.
- (92) Chazalviel, J. N.; Campagna, M.; Wertheim, G. K.; Shanks, H. R. *Phys. Rev. B* **1977**, *16*, 697.
- (93) Wertheim, G. K. *Chem. Phys. Lett.* **1979**, *65*, 377.
- (94) Wertheim, G. K.; Hufner, S. *Phys. Rev. Lett.* **1975**, *35*, 53.
- (95) Egdell, R. G.; Innes, H.; Hill, M. D. *Surf. Sci.* **1985**, *149*, 33.
- (96) Kim, Y. J.; Gao, Y.; Chambers, S. A. *Appl. Surf. Sci.* **1997**, *120*, 250.
- (97) Egdell, R. G.; Rebane, J.; Walker, T. J.; Law, D. S. L. *Phys. Rev. B* **1999**, *59*, 1792.
- (98) Payne, D. J.; Egdell, R. G.; Law, D. S. L.; Glans, P. A.; Learmonth, T.; Smith, K. E.; Guo, J. H.; Walsh, A.; Watson, G. W. *J. Mater. Chem.* **2007**, *17*, 267.
- (99) Yeh, J. J.; Lindau, I. *At. Data Nucl. Data Tables* **1985**, *32*, 1.
- (100) Glans, P. A.; Learmonth, T.; McGuinness, C.; Smith, K. E.; Guo, J. H.; Walsh, A.; Watson, G. W.; Egdell, R. G. *Chem. Phys. Lett.* **2004**, *399*, 98.
- (101) Glans, P. A.; Learmonth, T.; Smith, K. E.; Guo, J.; Walsh, A.; Watson, G. W.; Terzi, F.; Egdell, R. G. *Phys. Rev. B* **2005**, *71*, 235109.
- (102) Scanlon, D. O.; Walsh, A.; Morgan, B. J.; Watson, G. W.; Payne, D. J.; Egdell, R. G. *Phys. Rev. B* **2009**, *79*, 035101.

JP9093172